



A calibrated hydrogen-peroxide direct-borohydride fuel cell model

Richard O. Stroman ^{a, b, *}, Gregory S. Jackson ^c, Yannick Garsany ^d, Karen Swider-Lyons ^a

^a Chemistry Division, US Naval Research Laboratory, Washington DC 20375, United States

^b Department of Mechanical Engineering, University of Maryland, College Park, MD 20742, United States

^c Department of Mechanical Engineering, Colorado School of Mines, Golden, CO 80401, United States

^d EXCET Inc., 800 Braddock Road, Springfield, VA 22151, United States



HIGHLIGHTS

- A numerical model is developed for a H₂O₂-direct borohydride fuel cell (H₂O₂-DBFC).
- Global reactions in the model are calibrated vs. a simple experimental H₂O₂-DBFC.
- The calibrated model is used to predict the losses from parasitic side reactions.
- Maximum power density and system efficiency coincide due to parasitic side reactions.
- H⁺ reduction contributes to cathode current density when H₂O₂ is transport limited.

ARTICLE INFO

Article history:

Received 21 March 2014

Received in revised form

9 July 2014

Accepted 22 July 2014

Available online 31 July 2014

Keywords:

Fuel cell

Borohydride

Design

Transport

Power density

Reactant utilization

ABSTRACT

A numerical model with global reaction rates is calibrated to measurements from a simple hydrogen-peroxide direct-borohydride fuel cell (H₂O₂-DBFC), and then used to unravel complex electrochemical and competing parasitic reactions. In this H₂O₂-DBFC, fuel (1–50 mM NaBH₄/2 M NaOH) is oxidized at a Au anode and oxidizer (10–40 mM H₂O₂/1 M H₂SO₄) is reduced at a Pd:Ir cathode. Polarization curves and electrode potentials, as functions of fuel and oxidizer feeds support global reaction rate parameter fitting. The measurements and calibrated model showed H₂O₂ decomposition at the cathode depresses open circuit voltage from 3.01 V theoretical to 1.65 V, and when H₂O₂ supply is limited, cathode potentials are sufficiently negative to make H⁺ reduction to H₂ thermodynamically favorable. Calibrated model results show that thin concentration boundary layers limit reactant utilization and current density. Decreasing the inlet concentrations, flow rates, and cell voltage slow parasitic reactions and favor desirable charge transfer reactions. Peak conversion efficiency and peak power density coincide because thermodynamic efficiency and parasitic reaction rates decrease (relative to charge transfer reaction rates) with increasing current density. We conclude that the performance of a fuel cell with parasitic side reactions can be predicted through numerical modeling.

Published by Elsevier B.V.

1. Introduction

Direct borohydride fuel cells (DBFCs) have been considered for applications ranging from portable consumer electronics to vehicle propulsion. The term DBFC refers to diverse fuel cell configurations in which BH₄[−] is oxidized at the anode; review papers [1–8] summarize the variety of DBFC chemistries, catalysts and topologies explored to date. Two major classes include those utilizing acidic or alkaline oxidizer solutions. The DBFC studied herein uses NaBH₄/

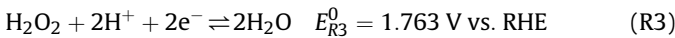
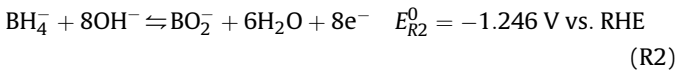
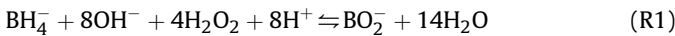
NaOH fuel and H₂O₂/H₂SO₄ oxidizer, and is referred to herein as a H₂O₂-DBFC.

This H₂O₂-DBFC offers several prospective advantages. First, the reactants can be stored at ambient temperature and pressure with concentrations of several molar, rather than as a high-pressure gas or cryogenic liquid. Second, when high reactant storage concentrations are combined with the 3.01 V theoretical cell potential for the NaBH₄/NaOH – H₂O₂/H₂SO₄ couple, the theoretical energy density and specific energy of the reactants surpass those of advanced Li-ion batteries [2]. Finally, DBFCs that consume stored H₂O₂ oxidizer can operate in anaerobic environments [9,10] (e.g. underwater or in space) and offer higher power density than systems that rely on O₂ due to the facile kinetics of H₂O₂ reduction.

* Corresponding author. Chemistry Division, US Naval Research Laboratory, Washington DC 20375, United States.

E-mail address: richard.stroman@nrl.navy.mil (R.O. Stroman).

The desired electrochemical reactions occurring in a H₂O₂-DBFC are written in (R1)–(R3). The net cell reaction (R1) consumes BH₄[−], H₂O₂, OH[−], and H⁺ and forms BO₂[−] and H₂O for a standard cell potential E_{R1}⁰ = 3.01 V. The anode and cathode half-cell reactions are in (R2) and (R3), respectively. In (R2), BH₄[−] and OH[−] are electrochemically oxidized to BO₂[−] and water. Electrons provided by (R2) travel through an external circuit to be consumed by the cathode half-cell electrochemical reduction of H₂O₂ and H⁺ (R3).



Parasitic chemical reactions can also occur; they uselessly consume reactants and depress cell voltage by shifting concentrations near the electrodes. At the anode catalyst, when the supply of OH[−] is insufficient, heterogeneous hydrolysis [11] converts BH₄[−] to BO₂[−] and H₂ via parasitic chemical reaction (R4).



Similarly, if the supply of H⁺ in the oxidizer solution is insufficient, H₂O₂ undergoes heterogeneous decomposition at the cathode catalyst [12–14] to form water via the parasitic chemical reaction (R5).



Reactions (R1)–(R5) each summarize multiple elementary intermediate steps. For example, transferring 8e[−] to the anode in reaction (R2) requires at least 8 elementary reactions. The microkinetics of elementary reactions occurring at a DBFC anode has been explored by Rostimikia et al. using density functional theory [15]. The rate determining elementary reactions and related kinetic parameters at the anode and cathode of a H₂O₂-DBFC are, however, still uncertain.

Experimental investigations of H₂O₂-DBFCs indicate that they do not meet their theoretical promise primarily because of transport limitations in the liquid reactant flow channels and the loss of fuel and oxidizer via parasitic chemical reactions at each electrode [11,16–19]. Unfortunately, the interdependences of the H₂O₂-DBFC electrochemistry and parasitic reactions are difficult to decouple experimentally because of their complexity. Carefully constructed numerical models are well suited to such problems, because they can capture the complexity while revealing parameters that are inaccessible experimentally. We previously developed a numerical model to understand the relationships between cell geometry, operating conditions, and performance in an ideal H₂O₂-DBFC where all reaction rates were fast and parasitic reactions were omitted [20,21]. For this present work, we revise the existing model to include realistic reaction rates and parasitic reactions. Experiments with a H₂O₂-DBFC guide selection of appropriate global reactions for the model, and provide measurements to which the model is calibrated. The model is calibrated by fitting kinetic terms in the global reaction rates to H₂O₂-DBFC polarization curves measured over a range of BH₄[−] concentrations. The simplified reaction mechanism in the revised model reduces the large number of uncertain kinetic parameters in comparison to elementary microkinetic models, and thereby makes fitting to measurements more tractable. With this simplification, the global reaction rates with fitted parameters can provide sufficient accuracy for cell-level

studies as long as they reasonably capture the rate-determining processes.

Following calibration against the experimental H₂O₂-DBFC, the model is used to investigate the effects of parasitic reactions on H₂O₂-DBFC performance by examining a baseline case and then departures from the baseline with variations in fuel inlet concentration and flow rate.

2. Model development

A steady state isothermal H₂O₂-DBFC having the form shown in Fig. 1 was modeled with a 2-D finite volume approach. Aqueous fuel (1–50 mM NaBH₄/2 M NaOH) and oxidizer (10–40 mM H₂O₂/1 M H₂SO₄) flow through rectangular channels separated by a Nafion 117 membrane. Catalyst-coated channel walls constrain the flows and act as electrodes. BH₄[−] is oxidized at the Au anode and H₂O₂ is reduced at the Pd:Ir cathode. Na⁺ cations cross the membrane to charge balance the cell, bringing H₂O with them via electro-osmotic drag. The geometry in Fig. 1 represents a class of DBFCs having separated electrodes and membranes. Such DBFCs have been considered in earlier studies [22,23] because they are simple to fabricate, resist precipitate accumulation, expose the full membrane to the aqueous electrolytes, and orient the electric field so that it aids reactant transport [21]. This DBFC configuration can be represented in a computationally efficient 2D model, when the channel sidewalls are inert (electrochemically inactive) and spaced widely enough to have negligible effect on the hydrodynamics of the reactant flows. The model predicts cell current when the cell geometry, inlet flow rates, inlet concentrations, and cell voltage are specified.

Only a summary of the transport calculations and solution approach are provided herein because they have been described previously [20,21]. The reaction mechanisms and rates are discussed in detail because they are specific to this study.

2.1. Transport in the channels and membrane

State variables describe the reactant solutions for computational cells in each flow channel: pressure P , velocities v_x and v_y , electric potential ϕ , and species mass fractions Y_k . For the fuel solution species, $k = \text{BH}_4^-$, BO₂[−], Na⁺, OH[−], H₂, or H₂O. For the oxidizer solution, $k = \text{H}_2\text{O}_2$, H⁺, Na⁺, SO₄^{2−}, H₂, O₂ or H₂O. The electrode-channel interfaces have state variables ϕ and Y_k , and the membrane–channel interfaces have state variables ϕ , Y_k and P . The value of each channel state variable is found by enforcing the associated conservation equation; conservation of mass (P), conservation of species (Y_k), conservation of momentum (v) and electroneutrality (ϕ). Solving for ϕ by enforcing electroneutrality implies that electrochemical double layers (the only regions in which substantial deviation from electroneutrality occur) are thin and effectively part of the electrode-channel interfaces. The interface values of P , ϕ , and Y_k are found by mass, charge and species flux matches, respectively. Fluxes due to electrode reactions and channel transport must match at electrode-channel interfaces, and fluxes due to membrane transport and channel transport must match at the membrane–channel interfaces. Mass, mole and charge densities are estimated using apparent molar solute volumes in the reactant solutions [21].

Boundary conditions at the inlets and outlets include fully developed momentum boundary layers ($\partial v_x / \partial x = 0$, $\partial v_y / \partial y = 0$) and no electric field in the x -direction ($\partial \phi / \partial x = 0$). Mass fractions are specified at the inlet (dictated by fuel and oxidizer concentrations) and pressure is specified at the outlet ($P = 0$). Boundary conditions at the electrodes include no-slip and impermeable boundary ($\nabla v = 0$, $\partial P / \partial y = 0$). The anode is assigned $\phi = 0$, making it the

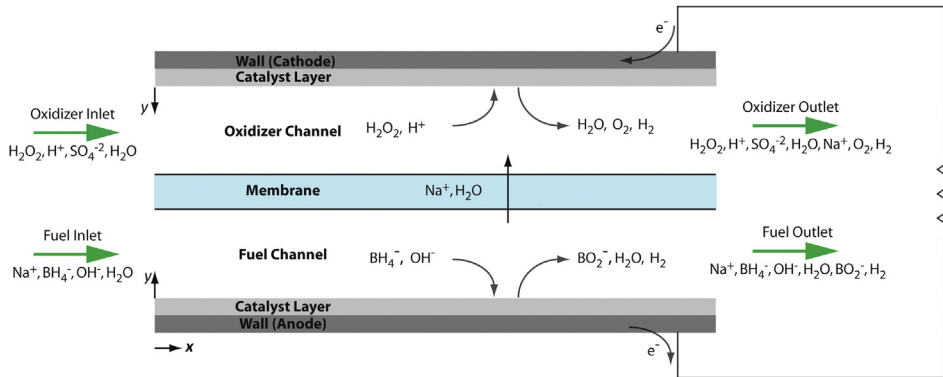


Fig. 1. Illustration of our DBFC cell configuration showing the cell geometry and major species flows, reactants, and products.

electric potential reference for the cell, and the cathode is assigned $\phi = V_{\text{cell}}$. The only boundary condition at the membrane is no-slip ($\partial v_x / \partial x = 0$).

Several simplifications are appropriate given the cell geometry and operating conditions. The reactant flows are laminar ($Re \ll 2300$), the cell is isothermal (heat capacities of reactant solutions are small compared to heating rate), the membrane is fully hydrated (in contact with aqueous solutions on both sides) and there are no homogenous reactions in the channel. All reactions occur at the catalyst/fluid interface. The reactant solutions are assumed to be ideal (i.e. activity coefficients $\gamma_k = 1$) because the activity coefficients for reactant species not in excess (BH_4^- and H_2O_2) vary little with concentration over the ranges examined in this study [24]. When $\partial \gamma_k / \partial C_k \approx 0$, non-idealities have little influence on the rates of transport [25].

2.2. Electrode reactions

The net rate of each charge transfer reaction at an electrode is modeled as the sum of anodic and cathodic rates as in Eq. (1), where the anodic direction provides electrons to the electrode and the cathodic direction removes them. The net rate depends on rate constants k , concentrations C_k , stoichiometric coefficients v , electric potential difference across the electrode-channel interface $\Delta\phi$, symmetry factors β , number of electrons transferred in the rate limiting step n_e , and $f = F/RT$. Net rates for chemical reactions omit the electric potential activation energy barriers by setting $n_e = 0$; in this case the anodic and cathodic rates simplify to forward and reverse rates as in Eq. (2). The nomenclature for symbols appearing in equations is summarized in Appendix A.

$$r = k_a \prod_k C_{k,a}^{v_{k,a}} e^{n_e \beta_a f \Delta\phi} - k_c \prod_k C_{k,c}^{v_{k,c}} e^{-n_e \beta_c f \Delta\phi} \quad (1)$$

$$r = k_f \prod_k C_{k,f}^{v_{k,f}} - k_r \prod_k C_{k,r}^{v_{k,r}} \quad (2)$$

Cathodic symmetry factors β_c are estimated as $\beta_c = 1 - \beta_a$ and n_e is assumed to be 1 based on the expectation that one elementary charge-transfer step (with single electron transfer) is likely rate-limiting for the overall reaction [26,27]. Concentrations C_k near the electrode and electric potential differences $\Delta\phi$ are provided by the transport portion of the model.

The net flux of each species k from an electrode, $\bar{J}_{k,\text{rxn}}$, is the sum of contributions from all reactions q at the electrode which involve species k , as shown in Eq. (3). A roughness parameter ℓ in

Eq. (3) adjusts the reaction fluxes based on the ratio of the active electrochemical surface area to the geometric electrode area.

$$\bar{J}_{k,\text{rxn}} = \ell \sum_q r_q v_{k,q} \quad (3)$$

Calibration experiments are used to fit rate parameters k_a and β_a for each electrochemical reaction, k_f for each chemical reaction, and ℓ for each electrode. Cathodic rate constants k_c are chosen to maintain thermodynamic consistency given the fitted values of k_a . Thermodynamic consistency in this case is defined as zero net rate for each reaction under standard conditions (1 M concentration, 298 K temperature, and 101.3 kPa pressure) at its equilibrium electrode potential. This is equivalent to solving $k_c = k_a e^{E^\circ}$.

To find values of k_a , β_a and ℓ that agree with the calibration experiments, a comparison function is developed. The comparison function calls the H_2O_2 -DBFC model code to generate a predicted polarization curve, and then calculates the difference (residual) between measured and predicted polarization curves at each cell potential. The MATLAB function *lsqnonlin* with a Newton search algorithm minimizes the L2-norm of the residuals by adjusting the fit parameters, k_a , β_a , and ℓ . The fit parameters are constrained to intervals $(0, \infty)$, $(0, 1]$ and $[1, 30]$ respectively. Trial and error with fit parameter initial guesses show that the initial guess must produce a polarization curve differing from the measurements by less than one order of magnitude or the fitting algorithm would likely find a local minimum. At least three widely spaced starting guesses are evaluated in each fitting effort, and the fit is not accepted as “final” until all three guesses result in the same fit, suggesting the fit may be global.

2.3. Calculating H_2O_2 -DBFC performance metrics

The H_2O_2 -DBFC performance is characterized herein by several metrics: reactant utilization, coulombic efficiency, thermodynamic efficiency, coulombic utilization, and conversion efficiency. These metrics describe the effectiveness with which reactants are used on a single pass through the cell, and the prospective performance improvement provided by recirculation, making them relevant to both single-pass and recirculated H_2O_2 -DBFCs. Furthermore, these metrics are strongly influenced by parasitic side reactions, which are present in both single-pass and recirculated H_2O_2 -DBFCs.

Reactant utilization $\eta_{\text{ru},k}$ is the fraction of reactant k consumed before the bulk flow carries it out of the cell. It is defined for the cell geometry in this study by Eq. (4), where L_{cell} is the channel length from inlet to outlet, $\bar{J}_{k,\text{elec}}$ is the local flux of reactant k to the electrode, $C_{k,\text{in}}$ is the concentration of k at the channel inlet and V_{in}

is the solution volumetric flow rate at the channel inlet. Fig. 1 shows that the x -coordinate runs from inlet to outlet.

$$\eta_{ru,k} = \frac{\int_0^{L_{cell}} \vec{J}_{k,elec} dx}{C_{k,in} \dot{V}_{in}} \quad (4)$$

Coulombic efficiency $\eta_{ce,k}$ is the fraction of consumed reactant k which contributes to the desired charge transfer reactions, and is a measure of losses to parasitic side reactions. It is calculated via Eq. (5), where i is local current density and v_e and v_k are the stoichiometric coefficients for electrons and species k in the charge transfer reaction(s), respectively. Average coulombic efficiency over the whole channel is $\bar{\eta}_{ce,k}$.

$$\eta_{ce} = \frac{i}{\vec{J}_{k,elec} v_e / v_k} \quad (5)$$

The thermodynamic efficiency, η_{th} , is the ratio of useful (electrical) work done by the fuel cell to the free energy change of the reactants. Thermodynamic efficiency is less than 1 due to activation losses at each electrode, mass transport and ohmic losses in each channel, and ohmic losses in the membrane. These losses are manifested as departures from the theoretical cell voltage (overpotentials), so the thermodynamic efficiency can be written as in Eq. (6).

$$\eta_{th} = V_{cell} / E_{R1}^0 \quad (6)$$

The reactant utilization, coulombic efficiency, and thermodynamic efficiency can be combined to form two other performance metrics. Coulombic utilization ($\eta_{cu,k} = \eta_{ru,k} \bar{\eta}_{ce,k}$) is the fraction of reactant k flowing into the cell which contributes to charge transfer reactions. Conversion efficiency for reactant k ($\eta_{c,k} = \eta_{th} \bar{\eta}_{ce,k}$) is the fraction of the chemical energy carried by reactant k into the H₂O₂-DBFC that is converted to electrical energy. Conversion efficiency, which depends on cell operating conditions and geometry, describes the amount of useful electrical energy that can be produced by a given quantity of reactant on a single pass through the H₂O₂-DBFC.

3. Experimental procedures

3.1. H₂O₂-DBFC fabrication

A H₂O₂-DBFC matching the geometry of Fig. 1 was designed and fabricated. The cell consisted of two flat graphite electrodes separated by flow channel masks and a Nafion 117 membrane (Fig. 2). The flow channel masks were 0.5 mm thick PTFE with 5 mm wide channels cut in them. The channels revealed a reactant port at each end, so that when the cell was assembled, reactants flowed through the channels. The regions of the graphite plates exposed to the flow channels each had an electrodeposited catalyst layer. Each graphite electrode was in contact with a gold-coated brass current collector. Holes through the entire assembly admitted bolts to compress and seal the cell; low reactant pressures simplified sealing. The compliance and hydrophobicity of the PTFE channel masks and the smoothness of the graphite plates together discouraged fluid entry between the layers. Large channel mask areas ensured dimensional stability in the direction perpendicular to the graphite plates so that the channel depth was dictated by the mask thickness. Channels were as wide as possible while supporting the membrane in the gap between the graphite plates. Components were selected to resist chemical attack by the corrosive reactant solutions. Aside

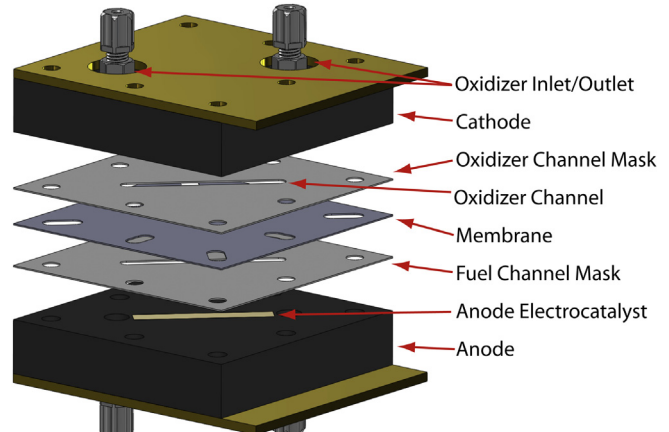


Fig. 2. Solid model of the DBFC used for calibration experiments. Fuel and oxidizer flow along the catalyst strip.

from the Nafion membrane and graphite electrodes, all wetted components were made of PTFE or PVDF.

Graphite electrodes were prepared for catalyst electrodeposition by rinsing with methanol and acetone, drying, and secondary rinsing with 18 MΩ water. The electrodes were sanded with coarse (P80 grit) Al₂O₃ sandpaper and then fine (P600 grit) SiC sandpaper, and resulting graphite powder was removed by sonication in an Ultrasonic Power Corp. model 5300/50-26-459 sonication bath for 20 min at 200 power (in bags with 18 MΩ water). Pre- and post-sonication micrographs showed that graphite dust was thoroughly removed.

The electrodeposition process was adapted from those described by Miley [28], de Leon [29], Urian [22] and Bessette [30]. Anode and cathode catalysts were deposited separately; in each case the cell was assembled with the electrode to receive the catalyst (working electrode, or WE), a graphite counter electrode (CE), a channel mask, and no membrane. The anode deposition solution consisted of 2 mM NaAuCl₄ and 200 mM NaCl in 18 MΩ water. The cathode solution consisted of 2 mM PdCl₂, 2 mM Na₃IrCl₆, 200 mM KCl and 0.1 M HCl in 18 MΩ water. Each was prepared using Alfa-Aesar Premion reagent grade salts. Solutions were circulated through the cell by a peristaltic pump. An Autolab PGSTAT30 potentiostat/galvanostat repeatedly drove current pulses (5 mA cm⁻² for 2.5 s and 0 mA cm⁻² for 2 s) through the cell while monitoring the WE potential with respect to a Ag/AgCl reference electrode (RE) in the beaker. The solution residence time in the cell was ~1 s, so this procedure replaced the solution between pulses. The number of pulses was chosen to give ~20 mg cm⁻² coverage (assuming 1:1 ratio for the Pd and Ir deposition rates). The inlet and outlet ports on the cell were reversed half-way through deposition to mitigate layer thickness variation from inlet to outlet. Deposition took place at room temperature (~23 °C). The procedures and results for electrochemical, chemical, and morphological characterization of the electrodes are provided as *Supplemental information*.

The Nafion 117 membrane was prepared by boiling in 3% H₂O₂ for 1 h to remove surface contaminants, then boiling in 1% NaOH for 1 h to convert to the Na⁺ form, and finally rinsing with 18 MΩ water.

3.2. H₂O₂-DBFC test stand setup

A test stand was built to control the flow of reactants through the cell and acquire data. The reactants were prepared as described in the *Supplemental information* section, and reactant solution

mass densities were measured to evaluate the accuracy of model predicted mass densities. The pH of reactant and effluent solutions was measured to determine whether H^+ and OH^- crossover must be included in the membrane model. Reactants began in carboys, and then flowed through the cell and an adjustable constriction used to control the flow rate. A combination of gravity and 17 kPa N_2 overpressure was used to drive the flows, ensuring consistent flow rate. The cell was operated with once-through (not recirculated) flows so that the inlet concentrations were known. Further details are given in the [Supplemental information](#) section.

A MACCOR Model 2300 test system was used to control and measure the cell voltage and current, and to record each electrode potential with respect to a Ag/AgCl reference electrode. MACCOR electric potential measurements were calibrated against an Autolab PGSTAT30 prior to the experiments. Cell temperature was measured by a K-type thermocouple affixed to the anode current collector. The same fuel and oxidizer flow rates were used for all experiments; they were measured twice per experiment by measuring the time to fill 250 mL graduated cylinders. Compiling all flow rate measurements gave $10.17 \pm 0.46 \text{ mL min}^{-1}$ for the fuel and $10.05 \pm 0.16 \text{ mL min}^{-1}$ for the oxidizer. The time measurement error was insignificant compared to the total time of ~25 min, so flow rate uncertainty depended on the graduated cylinder accuracy and flow rate variation.

3.3. Electrochemical evaluation of the H_2O_2 -DBFC

Polarization curves were measured by permitting the cell to equilibrate at open circuit and then stepping the cell potential from 0.4 V up to open circuit while measuring the current. Consistent results were obtained when the first step was held for 5 min to thoroughly reduce the cathode. Each subsequent cell potential was held for 2.5 min. The cell rapidly (<0.5 min) reached steady state after each cell potential change. Data were recorded at 1 Hz and an average current at each voltage step was compiled by averaging the last 2 min of the step. Three polarization curves were measured for each test condition and later compiled into an average curve with error bars marking one standard deviation.

Each set of polarization curve measurements began and ended with a baseline measurement to reveal changes in the cell state (for example, catalyst oxidation state). Baseline inlet concentrations were 10 mM $NaBH_4$ /2 M $NaOH$ fuel and 40 mM H_2O_2 /1 M H_2SO_4 oxidizer. This combination with 1:1 stoichiometry (assuming the ideal [reaction \(R1\)](#)) was chosen to make the baseline curves sensitive to changes at either electrode. Baseline curves varied little, indicating consistent cell state. Solution pH measurements before and after flowing through the H_2O_2 -DBFC, and solution density measurements are provided as [Supplemental information](#).

4. Results and discussion

4.1. H_2O_2 -DBFC experiments

The five polarization curves in [Fig. 3](#) (symbols) are measured with the H_2O_2 -DBFC operating at 1, 2.5, 5, 10, and 20 mM BH_4^- /2 M $NaOH$ fuel and 40 mM H_2O_2 /1 M H_2SO_4 oxidizer. The variant BH_4^- concentrations span the transition from fuel limited to oxidizer limited stoichiometry with respect to (R1). The fuel-limited case is studied with 1, 2.5 and 5 mM BH_4^- ; equivalent fuel:oxidizer at 10 mM BH_4^- ; and an oxidizer limited case with 20 mM BH_4^- . The reactant concentrations are lower than those in previously reported H_2O_2 -DBFC experiments [22,31,32] to minimize gas formation from BH_4^- hydrolysis and H_2O_2 decomposition and thereby maintain the validity of this single-phase flow model. The lower concentrations lead to lower power densities than in prior experiments. A

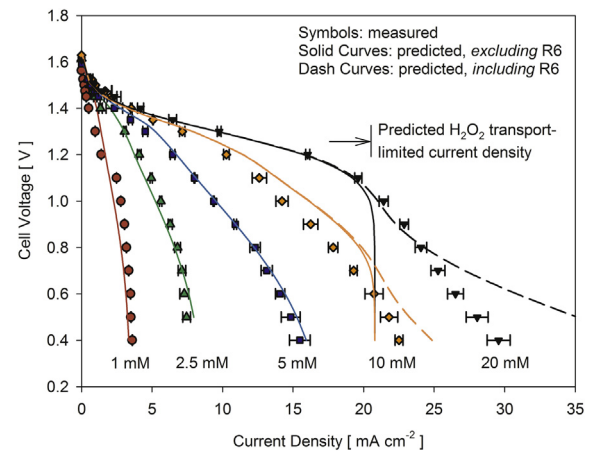


Fig. 3. Polarization curves with varying BH_4^- concentration/2 M $NaOH$ fuel, 40 mM H_2O_2 /1 M H_2SO_4 oxidizer, and both flow rates at 10 mL min^{-1} . Symbols are measured and curves are predicted after calibrating rate parameters to the measurements. Solid curves exclude [reaction R6](#) and dash curves include [reaction R6](#).

qualitative assessment of experimental data in [Fig. 3](#) indicates that BH_4^- transport limits appear in the fuel-limited 1, 2.5 and 5 mM BH_4^- curves with the current density tapering off at high current density, but curves measured in the oxidizer limited cases with 10 and 20 mM BH_4^- do not show the sharp drops in current density expected for H_2O_2 transport-limited behavior. This lack of H_2O_2 transport-limited behavior in the polarization curves is observed despite the greater diffusivity of BH_4^- ($2.42 \times 10^{-9} \text{ m}^2 \text{ s}^{-1}$) compared to H_2O_2 ($1.49 \times 10^{-9} \text{ m}^2 \text{ s}^{-1}$), which should make the H_2O_2 transport limit apparent at lower BH_4^- concentration.

The lack of an apparent H_2O_2 transport limit in [Fig. 3](#) is explained by H^+ reduction occurring at the cathode, which contributes to the total current density and has an onset potential that causes it to overlap with and obscure the H_2O_2 transport limit. H^+ reduction, written as [reaction \(R6\)](#), is thermodynamically favorable in acidic media at electrode potentials below 0.00 V vs. RHE [33].



Several observations support the conclusion that [reaction \(R6\)](#) is contributing to the cathode current density. First, the cathode potential falls below the limit of water stability in acidic media (line a_1 in [Fig. 4](#) [34]) at high current density, indicating [reaction \(R6\)](#) is

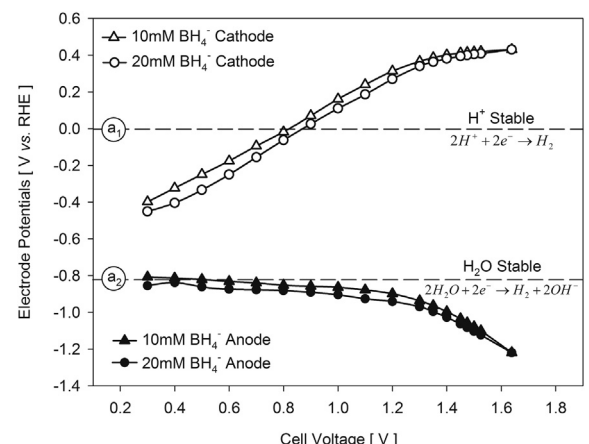


Fig. 4. Anode and cathode potentials measured vs. Ag/AgCl reference electrodes and then corrected to RHE.

thermodynamically favorable. Second, an *ex situ* experiment in which the cathode is placed in a bath of oxidizer solution and cycled through the same potential range as in the polarization curve measurements shows increased current density at potentials below 0.0 V vs. RHE and rapid gas production (presumably H₂) at potentials near −0.4 V vs. RHE. A plot of current density measured in the *ex situ* experiment is included as [Supplemental information](#). Finally, extending the 20 mM BH₄[−] polarization curve to 0.3 V shows an increase in current density ([Fig. 5](#)), commensurate with onset of reaction (R6) in oxidizer solution with ample H⁺. Reaction (R6) is included in the calibrated model because of these observations.

Onset of the H₂O₂ transport limit and reaction (R6) can be observed separately, in contrast to the 10 and 20 mM BH₄[−] curves of [Fig. 3](#), by measuring a polarization curve with a membrane having lower ohmic resistance. The lower membrane resistance does not affect the H₂O₂ transport limit, but does shift the onset of reaction (R6) to a lower cell potential. Since membrane ohmic resistance increases with time in DBFC experiments [31,35], this can be accomplished by comparing measurements with a fresh membrane to measurements with the original membrane that was used in prior experiments. A fresh vs. original membrane comparison is shown in [Fig. 5](#), where the decrease in cell potential at ~21 mA cm^{−2} for the fresh membrane is due to the H₂O₂ transport limit.

Measured electrode potentials, shown in [Fig. 4](#), can explain the difference between the theoretical 3.01 V OCP for reaction (R1) and the observed ~1.64 V OCPs in [Fig. 3](#). The measured anode OCP is 1.24 V vs. RHE, which is approximately equal to the expected value E_{R2}^0 . At the cathode, however, the measured OCP is 0.4 V vs. RHE which is much lower than the expected value E_{R3}^0 . The departure from theoretical OCP therefore occurs at the cathode, and is likely due to rapid heterogeneous H₂O₂ decomposition via reaction (R5). Consumption by reaction (R5) depresses the H₂O₂ concentration at the cathode-channel interface, and according to the Nernst equation, makes the equilibrium potential for reaction (R3) less positive. Rapid gas production (presumably O₂) at OCP is confirmed by placing the cathode in a bath of oxidizer solution.

4.2. Model calibration

The anode reaction mechanism consists of reactions (R2) and (R4), which have rates given by Eqs. (7) and (8). In Eq. (7), the first order dependence with respect to C_{BH₄} is supported by experimental evidence [36], and C_{BO₂} is included to maintain

thermodynamic consistency, despite the rate being relatively insensitive to C_{BO₂}. Likewise, the rate for reaction (R4) is effectively irreversible [36], so Eq. (8) lacks a reverse rate.

$$r_{R2} = k_{a,R2} C_{BH_4^-} e^{\beta_{a,R2} f \Delta \phi_a} - k_{c,R2} C_{BO_2^-} e^{-\beta_{c,R2} f \Delta \phi_a} \quad (7)$$

$$r_{R4} = k_{f,R4} C_{BH_4^-} \quad (8)$$

The cathode reaction mechanism consists of reactions (R3), (R5) and (R6) which have rates given by Eqs. (9)–(11).

$$r_{R3} = k_{a,R3} e^{\beta_{a,R3} f \Delta \phi_c} - k_{c,R3} C_{H_2O_2} e^{\beta_{c,R3} f \Delta \phi_c} \quad (9)$$

$$r_{R5} = k_{f,R5} C_{H_2O_2} \quad (10)$$

$$r_{R6} = k_{c,R6} C_{H^+}^2 e^{2\beta_{a,R6} f \Delta \phi_c} - k_{c,R6} C_{H_2} e^{-2\beta_{c,R6} f \Delta \phi_c} \quad (11)$$

The second-order dependence on C_{H⁺} and n_e = 2 in Eq. (11) imply that the rate limiting step for reaction (R6) is H⁺ accepting an electron, which must occur twice. The concentration of H⁺ was included in Eq. (11), despite H⁺ being in excess, because it was the only reactant in the rate equation and omitting it would have permitted a “runaway” reaction with no H⁺ present. While this cannot occur in the real cell, it could have caused numerical problems when solving the model.

The parameter fitting process yields the values in [Table 1](#). The predicted polarization curves are compared to the measured curves in [Fig. 3](#), which shows good agreement for the BH₄[−] limited stoichiometries (R² values of 0.920, 0.986, and 0.996 for 1, 2.5 and 5 mM BH₄[−] curves, respectively) and reasonable, but less accurate, predictions for the H₂O₂ limited stoichiometries. The fitted rate parameters for reactions (R2) and (R3) are not directly comparable to the values reported by Santos [37] and Finkelstein [38,39], because these authors reported rates in terms of overpotential rather than the electrode-interface potential differences used here. Furthermore, Finkelstein calculated overpotentials by assuming the equilibrium potential for each reaction was equal to the observed onset potential. Nevertheless, the fitted rate parameters are similar to the reported values. Finkelstein reported $k_{a,R2} = 6.2 \times 10^{-4}$ m s^{−1} and $\beta_{a,R2} = 0.2$ on Au for 5 mM NaBH₄ in 1 M NaOH, and $k_{c,R3} = 8 \times 10^{-3}$ m s^{−1} and $\beta_{c,R3} = 0.45$ on Pt for 5 mM H₂O₂ in 0.5 M H₂SO₄.

The fit between the predicted and measured polarization curves with 20 mM BH₄[−] (dash lines in [Fig. 3](#)) could not be improved with the reaction rate for (R6) written as in Eq. (11). The discrepancy at low cell voltage may be due in part to the lack of competition for catalyst surface sites in Eq. (11). The adsorption of OH plays a major role in H₂O₂ reduction [40] and the onset of significant H⁺ reduction could be delayed to a lower cathode potential by competition with surface adsorbed OH occupying sites on the Pd:Ir surface, although this study yielded no direct evidence to support this hypothesis.

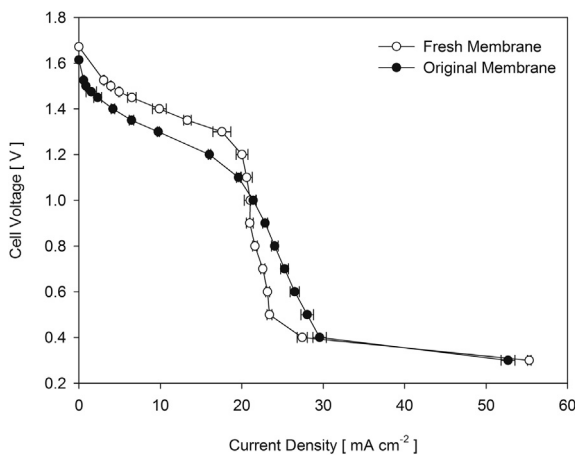


Fig. 5. Measured 20 mM BH₄[−] polarization curves; “Original Membrane” is replotted here from [Fig. 3](#), but with a point at 0.3 V cell that was omitted in [Fig. 3](#).

Table 1
Fitted rate parameters for reactions R2 through R6.

Anode parameters	Cathode parameters
$k_{a,R2}$	9.25×10^{-3} m s ^{−1}
$\beta_{a,R2}$	0.098
$k_{f,R4}$	3.09×10^{-4} m s ^{−1}
ℓ_a	2.73
	$k_{c,R3}$
	7.54×10^{-3} m s ^{−1}
	$\beta_{c,R3}$
	0.455
	$k_{f,R5}$
	6.34×10^{-4} m s ^{−1}
	$k_{c,R6}$
	1.19×10^{-9} m ⁴ kmol ^{−1} s ^{−1}
	$\beta_{c,R6}$
	0.141
	ℓ_c
	4.11

Comparing the model predictions to measured transport-limited current densities indicate that the model correctly predicts the rates of reactant transport to the electrodes. The model and experiments agree at low cell potential for the for the BH_4^- limited stoichiometries in Fig. 3 (1, 2.5, and 5 mM BH_4^- curves) showing that the model accurately predicts the rates of BH_4^- transport to the anode. Turning off reaction (R6) reveals that the model predicts an H_2O_2 transport limited current density of $\sim 21 \text{ mA cm}^{-2}$ (solid 10 and 20 mM BH_4^- curves in Fig. 3), in agreement with the measurements shown in Fig. 5 (“fresh membrane”), showing the model accurately predicts the rate of H_2O_2 transport to the cathode.

4.3. Results from the calibrated model

A series of simulations with the calibrated model were used to examine the influences of parasitic reactions, cell geometry, and operating conditions on H_2O_2 -DBFC performance. H_2O_2 -DBFC performance in each simulation was characterized by $\eta_{\text{ru},k}$, $\eta_{\text{ce},k}$, η_{th} , and power density. The baseline case includes 50 mM NaBH_4 /2 M NaOH fuel, 250 mM H_2O_2 /1 M H_2SO_4 oxidizer, and flow rates of 10 mL min^{-1} . These conditions were chosen for three reasons. First, the baseline concentrations are higher than in the calibration experiments, and therefore closer to the concentrations that might be used in a practical H_2O_2 -DBFC, but still low enough for limited gas production, which preserves the validity of the incompressible and laminar flow simplifications. Second, the baseline concentrations have nearly 1:1 stoichiometry and should therefore reveal losses at both electrodes. Finally, the baseline H_2O_2 concentration is sufficient to avoid significant H^+ reduction at the cathode, so baseline simulations address operating conditions for which the calibrated model is most accurate.

4.3.1. Effects of parasitic reactions

Losses due to parasitic reactions are manifested in two ways: loss of reactants to gas production (lower $\eta_{\text{ce},k}$), and lower cell potential via the Nernst equation as reactant concentrations near the electrodes are depressed (lower η_{th}). Cell potentials predicted by the calibrated model with BH_4^- hydrolysis (reaction (R5)) and H_2O_2 decomposition (reaction (R6)) turned on are lower than those predicted with these reactions turned off, as shown in Fig. 6. Both curves in Fig. 6 are plotted at 100 mA cm^{-2} current density to make ohmic losses comparable, evidenced by both curves having the same electric potential gradient in the membrane. The predicted power density with reactions (R5) and (R6) is 80 mW cm^{-2} ,

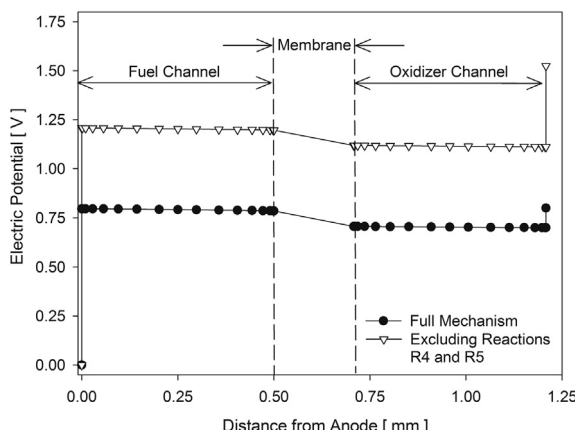


Fig. 6. Electric potential profiles across the cell predicted by the calibrated model, at the midpoint (25 mm from the inlets), for the baseline case at 100 mA cm^{-2} current density. The two curves compare results with reactions R4 and R5 turned on and off.

whereas the predicted power density without them is nearly twice as high at 152 mW cm^{-2} .

The predicted effects of gas production and depressed cell potential on the anode are plotted in Fig. 7, which shows that the fuel conversion efficiency $\eta_{\text{ce},\text{BH}_4^-}$ has a peak due to opposing trends in $\eta_{\text{ce},\text{BH}_4^-}$ and η_{th} . The cell power density is included in Fig. 7 to show that peak fuel conversion efficiency coincides with peak power. The most energy can therefore be extracted from a limited fuel supply by operating the cell at peak power, in contrast to most other fuel cells, such as PEMFCs, which do not suffer from parasitic side reactions. The most efficient operating point for a PEMFC is near OCP because thermodynamic efficiency is greatest near OCP. The model predicts that peak oxidizer conversion efficiency also coincides with peak power density.

Predicted η_{ce} increases with current density, and two explanations are plausible. First, increasing current density leads to lower cell potential and therefore smaller activation energy barriers for charge transfer reactions. This favors charge transfer reactions, which then outcompete chemical parasitic reactions for reactants at the electrode-channel interfaces. Second, high current density leads to lower reactant concentrations at the electrode-channel interfaces as stronger concentration boundary layers develop in response to higher reactant consumption rates. The rates of parasitic chemical reactions are more sensitive to reactant concentration, and thus, they slow more than the charge transfer reactions in response to the reduced concentrations.

4.3.2. Influence of cell geometry

The rates of gas production by the parasitic reactions (R5) and (R6), and the net current density, are plotted with respect to distance from the inlets in Fig. 8(a). Gas production rates and current density both decrease with distance from the inlet, as concentration boundary layers develop and limit concentrations at the electrode-solution interface. The predicted gas production rates are credible because they depend on fitted reaction rate parameters and aqueous species transport for which the diffusion, migration, and advection fluxes can be estimated accurately. The predicted rates of H_2 and O_2 transport in the channel, however, are likely in error because the predicted concentrations exceed the saturation limits for these species in water. The saturation limit of H_2 in pure water at 298 K is $7.8 \times 10^{-4} \text{ M}$, and the saturation limit of O_2 in 1 M H_2SO_4 is $9.3 \times 10^{-4} \text{ M}$ [41]. Higher concentrations imply bubble formation and because the model does not include multiphase

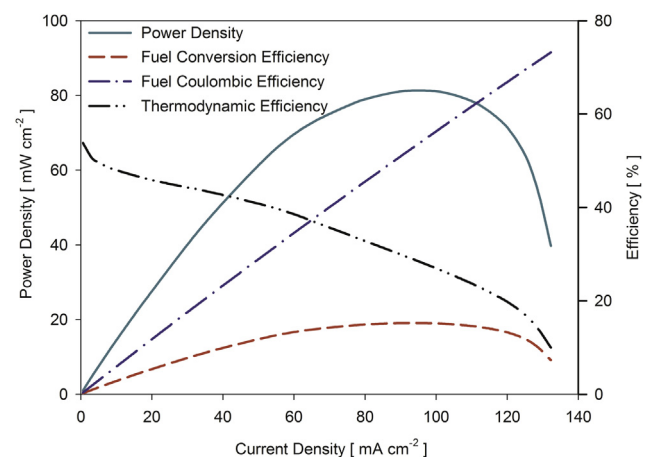


Fig. 7. Effective fuel conversion efficiency, plotted with coulombic and thermodynamic efficiencies to show how conversion efficiency is the result of opposing trends, and plotted with power density to show that peak conversion efficiency and peak power density coincide.

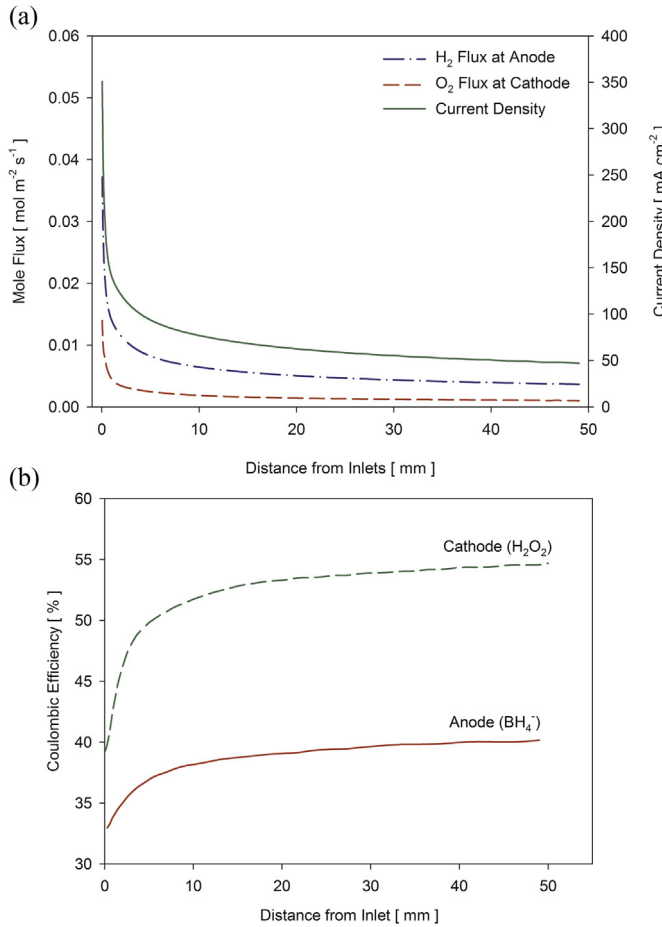


Fig. 8. (a) Predicted current density and H₂ and O₂ production rates with respect to position in the channel. (b) Influence of the H₂ and O₂ production rates on the coulombic efficiency. Both plots show the 50 mM NaBH₄/250 mM H₂O₂ baseline case at 1.1 V cell and 10 mL min⁻¹.

flow, predicted gas concentrations are useful only as indicators of likely bubble formation. Most bubbles should form near the inlets due to the preponderance of gas production there; this insight could be useful for the design of graded catalyst structures which discourage bubble adhesion near the inlets and emphasize reactant access to the catalyst at points further from the inlet.

Fig. 8(b) plots predicted η_{ce} with respect distance from the inlets and shows that for these operating conditions, the cathode delivers electrons to H₂O₂ more effectively than the anode extracts electrons from BH₄. More than 50% of the H₂O₂ flux to the cathode is electrochemically reduced but less than 40% of the BH₄⁻ flux to the anode is electrochemically oxidized. Low overall η_{ce} suggests that future research should aim to shift the relative rates of reaction more in favor of charge transfer reactions. One approach is to develop novel catalyst materials and morphologies [19], but another is to choose operating conditions which favor charge transfer reactions. Among the operating conditions that can be changed to favor charge transfer reactions are the cell voltage, inlet concentrations, and fuel and oxidizer flow rates.

4.3.3. Influence of cell voltage

Cell voltage can be controlled to achieve higher η_{ce} . The coulombic efficiencies of the anode and cathode for the baseline case are plotted with respect to cell potential in Fig. 9, which shows that lower cell potentials increase η_{ce} at both electrodes. In effect, lower cell potential decreases the activation energy barriers to

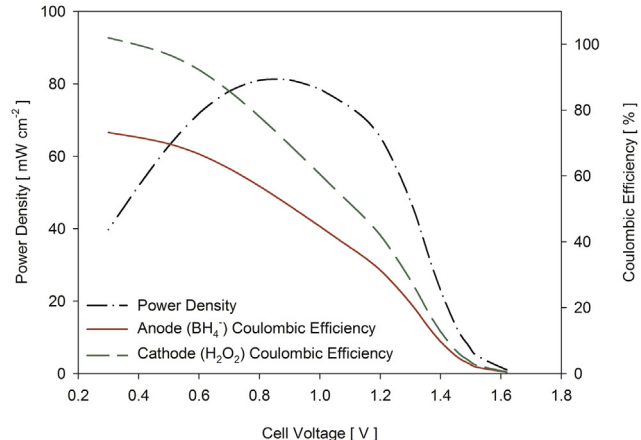


Fig. 9. Predicted power density and coulombic efficiency for 50 mM BH₄/250 mM H₂O₂ with 10 mL min⁻¹ flow rates.

charge transfer reactions and therefore increases their rates. The rates of parasitic side reactions do not depend on potential, and so their rates decline relative to charge transfer reactions for reactants at the electrode interfaces.

Power density is included in Fig. 9 to show the relationship between η_{ce} and the desirable operating envelope of the fuel cell. Since V_{cell} falls with increasing power density, η_{ce} rises with increasing power density. Gains in η_{ce} beyond the peak power point are undesirable, however, because they coincide with falling η_{th} and are accompanied by greater total reactant fluxes to the electrodes. Beyond the peak power point, any gains in η_{ce} are offset by overall efficiency losses and greater reactant consumption rates, thus the maximum desirable η_{ce} is at peak power.

Coulombic utilization, η_{cu} , is greater at the anode because the diffusivity of BH₄⁻ (2.42×10^{-9} m²s⁻¹ [42]) is larger than H₂O₂ (1.19×10^{-9} m²s⁻¹ [24]) and because BH₄⁻ transport is aided by migration [21]. The fuel and oxidizer coulombic utilizations both show trends with respect to V_{cell} which are similar to the trends in Fig. 9 for η_{ce} . The generally slow reactant transport through aqueous solution leads to low η_{cu} (<4%) for both sides of the cell under these operating conditions.

4.3.4. Influences of fuel flow rate and inlet concentration

H₂O₂-DBFC analysis without parasitic reactions has shown that raising reactant flow rates improved power density and η_{th} through increased convection mass transport in the channels [21]. The same is true when parasitic reactions are included, but with a caveat. The higher rates of transport to the electrodes also lead to higher rates of gas production. The influence of fuel flow rate on concentration boundary layer development is shown in Fig. 10, where the BH₄⁻ concentration boundary layer at 10 mL min⁻¹ fuel flow rate is compact and the boundary layer at 1 mL min⁻¹ is beginning to envelop the entire channel. The compact boundary layer is the result of convection augmenting the rate of diffusion mass transport to the anode.

Variation in peak power density among curves in Fig. 11(a) shows how greater power density incurs a lower upper bound on coulombic efficiency. As fuel flows more quickly, BH₄⁻ concentration at the anode interface rises in response to more facile transport from the bulk. Higher BH₄⁻ concentration favors hydrolysis, so coulombic efficiency falls. Peak power density approaches the horizontal axis with decreasing flow rate until it intercepts the axis at zero flow rate. The maximum theoretical coulombic efficiency for these operating conditions is ~73% and occurs in the zero flow rate

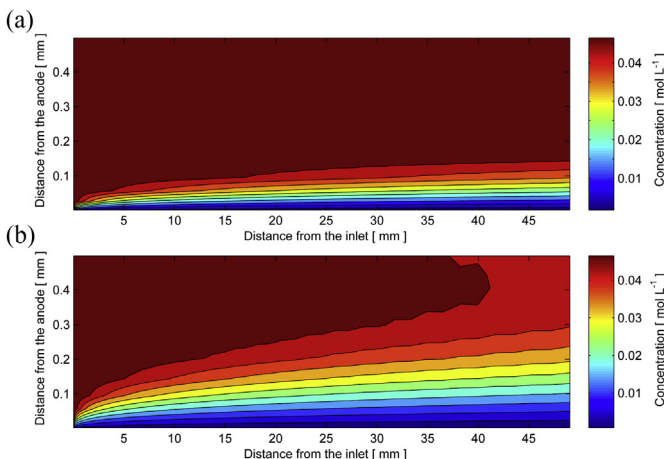


Fig. 10. Predicted BH_4^- concentration in the fuel channel for the baseline case at 1.1 V for (a) 10 mL min^{-1} and (b) 1 mL min^{-1} flow rates. Both plots share the same color map. (For interpretation of the references to colour in this figure legend, the reader is referred to the web version of this article.)

case, where diffusion and migration alone dictate the rates of transport to the anode. The power density shows a different relationship with respect to coulombic utilization. In Fig. 11(b), peak power density asymptotically approaches zero as the coulombic utilization approaches 100%.

The influence of inlet concentration on H_2O_2 -DBFC performance is examined with respect to the concentration of BH_4^- . Changing the inlet concentration revealed a relationship between power density and coulombic efficiency which mirrors that of the fuel flow rate. Increases in fuel flow rate and inlet concentration both shift the relative rates of reaction at the anode in favor of H_2 production by increasing BH_4^- concentration at the anode interface. The coulombic utilization trend with respect to BH_4^- concentration differs from the trend with respect to flow rate. Slower flow rates increase residence times in the H_2O_2 -DBFC while diffusion and migration continue to transport BH_4^- to the anode, leading to the asymptotic approach to zero power density at 100% coulombic utilization seen in Fig. 11(b). Lower inlet concentrations decrease the rate of transport by all three processes (migration, diffusion, and convection), leading to a theoretical upper bound of ~4.75% coulombic utilization at zero inlet concentration.

5. Conclusions

We show that global reactions and rates, if properly calibrated, can describe borohydride oxidation and hydrogen peroxide reduction with sufficient accuracy for H_2O_2 -DBFC design analysis. The finite volume approach applied to modeling transport in a H_2O_2 -DBFC accurately predicts the fluxes of ions and neutral species in the reactant solutions, without the complexity of a non-ideal electrolyte model, for the operating conditions examined in the experiments.

A numerical model calibrated to a simple H_2O_2 -DBFC shows that the limited diffusivities and mobilities of reactants in aqueous solution are responsible for the development of compact boundary layers and low single-pass reactant utilization. The relative rates of charge transfer reactions and parasitic reactions are shifted in favor of charge transfer by lower reactant concentrations near the electrodes and larger activation overpotentials. These conditions can be achieved by lower reactant inlet concentrations, slower bulk flows in the channels, and operating the cell at high current density (low cell voltage). The opposite trends in cell coulombic efficiency and thermodynamic efficiency with respect to current density lead to a peak overall efficiency point which (for the cell geometry and operating conditions examined in this study) coincides with peak power density. The coincidence of peak conversion efficiency and peak power distinguishes H_2O_2 -DBFCs from fuel cell technologies that are less strongly affected by parasitic electrode reactions. The insight into H_2O_2 -DBFC behavior provided by the numerical model illustrates the utility of such models for cell design and selection of appropriate operating parameters when complex chemistry and transport processes complicate performance prediction.

In future work, the demonstrated modeling approach could be applied to other electrochemical systems, including alternative H_2O_2 -DBFCs utilizing alkaline oxidizer solutions and anion-exchange membranes. The transport and membrane sub-models would be modified to include alternative species (HO_2^- in the case of an alkaline oxidizer solution and OH^- in the case of an anion-exchange membrane) and the cathode reaction rate sub-model would be adapted to a different reaction mechanism. The governing equations, solution approach, and calibration methods would remain the same.

Acknowledgments

The authors gratefully acknowledge the support of the NRL Edison Memorial Training Program, the NRL Chemistry Division, and the Office of Naval Research for their support of this work.

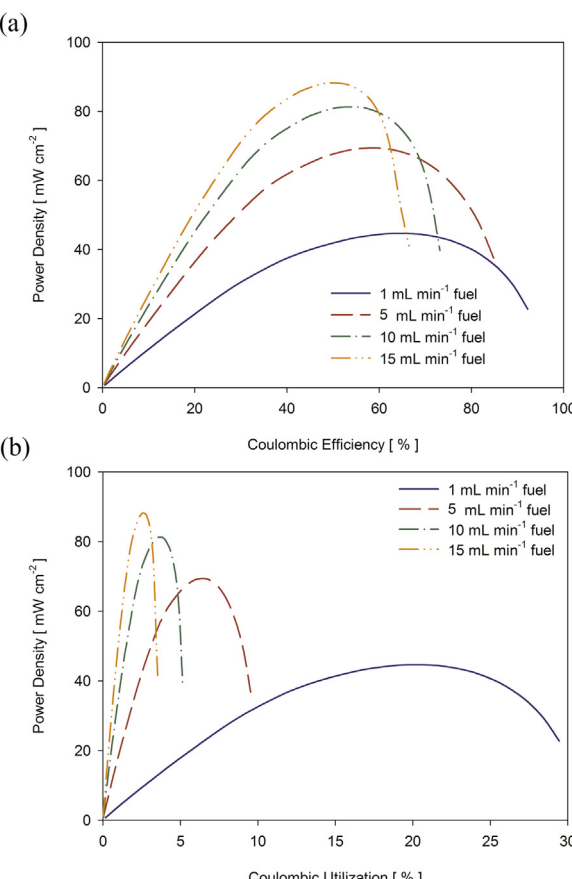


Fig. 11. Predicted (a) coulombic efficiency (b) and coulombic utilization. Both plots share fuel flow rates from 1 to 15 mL min^{-1} , oxidizer flow rate of 10 mL min^{-1} , and $50 \text{ mM } \text{BH}_4^-/250 \text{ mM } \text{H}_2\text{O}_2$.

Appendix A. Nomenclature

a	anodic parameter (subscript)
β	electrochemical reaction symmetry factor
c	cathodic parameter (subscript)
C_k	concentration of species k
E_R^0	standard half-cell potential for reaction R
F	Faraday's constant
f	$F/R_{ig}T$
i	current density
\overrightarrow{J}	mass flux
$\overrightarrow{J}_{k,\text{elec}}$	flux of species k to an electrode
\overrightarrow{J}_k	mole flux of species k
k_q	rate constant for reaction q
ℓ	roughness factor
L_{cell}	length of flow channels from inlet to outlet
$\eta_{ru,k}$	reactant utilization with respect to species k
η_{th}	thermodynamic efficiency
$\eta_{cu,k}$	coulombic utilization
η_{ce}	coulombic efficiency
$\eta_{c,k}$	conversion efficiency with respect to species k
n_e	number of e^- in rate limiting reaction step
n_{elec}	number of e^- transferred per mole of reactant consumed
ϕ	electric potential
P	pressure
ρ	solution mass density
ρ_c	net charge density
R_{ig}	ideal gas constant
r_q	rate of reaction q
T	temperature
u_k	mobility of species k
v_x, v_y	velocity in x - and y - directions
$v_{k,q}$	stoichiometric coefficient of species k in reaction q
V	volumetric flow rate
x	coordinate axis parallel to membrane
y	coordinate axis perpendicular to membrane
Y_k	mass fraction of species k
z_k	charge number of species k
γ_k	activity coefficient for species k

Appendix B. Supplementary data

Supplementary data related to this article can be found at <http://dx.doi.org/10.1016/j.jpowsour.2014.07.139>.

References

- [1] C.P. de Leon, F.C. Walsh, D. Pletcher, D.J. Browning, J.B. Lakeman, *J. Power Sources* 155 (2006) 172–181.
- [2] I. Merino-Jimenez, C.P. de Leon, A.A. Shah, F.C. Walsh, *J. Power Sources* 219 (2012) 339–357.
- [3] J. Ma, N.A. Choudhury, Y. Sahai, *Renew. Sust. Energy Rev.* 14 (2010) 183–199.
- [4] U.B. Demirci, *J. Power Sources* 172 (2007) 676–687.
- [5] R. Retnamma, A.Q. Novais, C.M. Rangel, *Int. J. Hydrogen Energy* 36 (2011) 9772–9790.
- [6] D.M.F. Santos, C.A.C. Sequeira, *Renew. Sust. Energy Rev.* 15 (2011) 3980–4001.
- [7] B.H. Liu, Z.P. Li, *J. Power Sources* 187 (2009) 291–297.
- [8] G.H. Miley, N. Luo, J. Mather, R. Burton, G. Hawkins, L.F. Gu, E. Byrd, R. Gimlin, P.J. Shrestha, G. Benavides, J. Laystrom, D. Carroll, *J. Power Sources* 165 (2007) 509–516.
- [9] N. Luo, G.H. Miley, K.J. Kim, R. Burton, X.Y. Huang, *J. Power Sources* 185 (2008) 685–690.
- [10] J.B. Lakeman, A. Rose, K.D. Pointon, D.J. Browning, K.V. Lovell, S.C. Waring, J.A. Horsfall, *J. Power Sources* 162 (2006) 765–772.
- [11] B.H. Liu, J.Q. Yang, Z.P. Li, *Int. J. Hydrogen Energy* 34 (2009) 9436–9443.
- [12] V.R. Choudhary, A.G. Gaikwad, *React. Kinet. Catal. L* 80 (2003) 27–32.
- [13] V.R. Choudhary, C. Samanta, T.V. Choudhary, *J. Mol. Catal. A-Chem* 260 (2006) 115–120.
- [14] A.J. Hung, S.F. Tsai, Y.Y. Hsu, J.R. Ku, Y.H. Chen, C.C. Yu, *Int. J. Hydrogen Energy* 33 (2008) 6205–6215.
- [15] G. Rostamikia, A.J. Mendoza, M.A. Hickner, M.J. Janik, *J. Power Sources* 196 (2011) 9228–9237.
- [16] Z.P. Li, B.H. Liu, J.K. Zhu, S. Suda, *J. Power Sources* 163 (2006) 555–559.
- [17] H. Senoh, Z. Siroma, N. Fujiwara, K. Yasuda, *J. Power Sources* 185 (2008) 1–5.
- [18] M. Chatenet, F.H.B. Lima, E.A. Ticianelli, *J. Electrochem. Soc.* 157 (2010) B697–B704.
- [19] K.S. Freitas, B.M. Concha, E.A. Ticianelli, M. Chatenet, *Catal. Today* 170 (2011) 110–119.
- [20] R.O. Stroman, Understanding Direct Borohydride-Hydrogen Peroxide Fuel Cell Performance, 318pp., University of Maryland, College Park MD, 2013.
- [21] R.O. Stroman, G.S. Jackson, *J. Power Sources* 247 (2014) 756–769.
- [22] R.C. Urian, C.J. Patrissi, S.P. Tucker, C.M. Deschenes, F.W. Bielwski, D.W. Atwater, in: Proceedings of the 43rd Power Sources Conference, vol. 43, 2008, pp. 295–298.
- [23] R.C. Urian, in: Material Research Society Symposium Proceedings, vol. 1213, 2010.
- [24] W.C. Schumb, *Hydrogen Peroxide*, Reinhold Pub. Corp., New York, 1955.
- [25] R.B. Bird, W.E. Stewart, E.N. Lightfoot, *Transport Phenomena*, second ed., Wiley international ed., J. Wiley, New York, 2002.
- [26] G. Rostamikia, M.J. Janik, *J. Electrochem. Soc.* 156 (2009) B86–B92.
- [27] J.S. Newman, K.E. Thomas-Alyea, *Electrochemical Systems*, third ed., J. Wiley, Hoboken, NJ, 2004.
- [28] L.F. Gu, N. Luo, G.H. Miley, *J. Power Sources* 173 (2007) 77–85.
- [29] C.P. de Leon, F.C. Walsh, C.J. Patrissi, M.G. Medeiros, R.R. Bessette, R.W. Reeve, J.B. Lakeman, A. Rose, D. Browning, *Electrochim. Commun.* 10 (2008) 1610–1613.
- [30] R.R. Bessette, J.M. Cichon, D.W. Dischert, E.G. Dow, *J. Power Sources* 80 (1999) 248–253.
- [31] C.P. de Leon, F.C. Walsh, A. Rose, J.B. Lakeman, D.J. Browning, R.W. Reeve, *J. Power Sources* 164 (2007) 441–448.
- [32] R.K. Raman, N.A. Choudhury, A.K. Shukla, *Electrochim. Solid St.* 7 (2004) A488–A491.
- [33] M. Pourbaix, *Atlas of Electrochemical Equilibria in Aqueous Solutions*, second English ed., National Association of Corrosion Engineers, Houston, Tex, 1974.
- [34] A.A. Kulikovsky, *J. Appl. Electrochem.* 30 (2000) 1005–1014.
- [35] D.M.F. Santos, C.A.C. Sequeira, *J. Electrochim. Soc.* 159 (2012) B126–B132.
- [36] H. Cheng, K. Scott, *Electrochim. Acta* 51 (2006) 3429–3433.
- [37] D.M.F. Santos, C.A.C. Sequeira, *J. Electrochim. Soc.* 156 (2009) F67–F74.
- [38] D.A. Finkelstein, N. Da Mota, J.L. Cohen, H.D. Abruna, *J. Phys. Chem. C* 113 (2009) 19700–19712.
- [39] D.A. Finkelstein, J.D. Kirtland, N. Da Mota, A.D. Stroock, H.D. Abruna, *J. Phys. Chem. C* 115 (2011) 6073–6084.
- [40] B.D. Adams, C.K. Ostrom, A.C. Chen, *J. Electrochim. Soc.* 158 (2011) B434–B439.
- [41] D.R. Lide, *CRC Handbook of Chemistry and Physics*, Chapman and Hall/CRCnetBASE, Boca Raton, FL, 1992.
- [42] D.M.F. Santos, C.A.C. Sequeira, *J. Electrochim. Soc.* 157 (2010) F16–F21.